Nanoclay-reinforced alginate/salecan composite inks for 3D printing applications

Raluca Ianchis[1], Maria Minodora Marin[2,3]*, Rebeca Leu Alexa[2]*, Ioana Catalina Gifu[1], Elvira Alexandrescu[1], Gratiela Gradisteanu Pircalabioru[4,5,6], George Mihail Vlasceanu[2], George Mihail Teodorescu[1], Andrada Serafim[2], Silviu Preda[7], Cristina Lavinia Nistor[1], and Cristian Petcu[1]

[1]National Research & Development Institute for Chemistry and Petrochemistry, ICECHIM, Spl. Independentei No. 202, 6th District, 060021 Bucharest, Romania

[2]Advanced Polymer Materials Group, Politehnica University of Bucharest, 1-7 Polizu Street, 011061 Bucharest, Romania

[3]Collagen Department, Leather and Footwear Research Institute, 93 Ion Minulescu Street, 031215 Bucharest, Romania

[4]eBio-hub Research Center, University Politehnica of Bucharest - CAMPUS, 6 Iuliu Maniu Boulevard, 061344 Bucharest, Romania

[5]Research Institute of University of Bucharest (ICUB), University of Bucharest, Bucharest, Romania

[6]Academy of Romanian Scientists, Bucharest, Romania

[7]Institute of Physical Chemistry "Ilie Murgulescu", Romanian Academy, Spl. Independentei 202, 6th District, 060021 Bucharest, Romania

*Corresponding authors:
Maria Minodora Marin
(maria_minodora.marin@upb.ro)

Rebeca Leu Alexa
(rebeca.leu@upb.ro)

Abstract

The main objective of the present work was to produce three-dimensional (3D)-printable nanocomposite hydrogels based on two kinds of marine-sourced polysaccharides doped with nanoclay with potential biomedical application. First part of the research study investigated the preparation of the polysaccharide bicomponent hydrogel formulations followed by the selection of the optimal ratio of polysaccharides concentrations which ensured proper morphostructural stability of the 3D-printed constructs. Second step aimed to generate 3D scaffolds with high printing fidelity by modulating the nanoclay amount doped within the previously selected biopolymer ink. In compliance with the additive manufacturing experiments, the alginate–salecan hydrogels enriched with the highest nanofiller concentrations demonstrated the highest suitability for 3D printing process. The morphological and structural studies confirmed the ability of the nanocomposite formulations to efficiently produce porous 3D-printed constructs with improved fidelity. The morphostructural findings underlined the implication of choosing the appropriate ratio between components, as they have a considerable impact on the functionality of printing formulations and subsequent 3D-printed structures. Hence, from the obtained results, these novel hydrogel nanocomposites inks are considered valuable biomaterials with suitable features for applications in the additive manufacturing of 3D structures with precise shape for customized regenerative therapy.

Keywords: Alginate; Salecan; Hydrogel; Nanocomposites; 3D printing

1. Introduction

In order to address a variety of biological problems, current research studies are focused on developing multicomponent and multifunctional composite scaffolds employing a variety of material combination and design.

The oceans are a major renewable supply of natural chemicals and contain a diversity of compounds. Polysaccharides are abundant in the marine ecosystem, and their corresponding biological and physicochemical characteristics have encouraged their use for the creation of a wide range of biomaterials in the form of hydrogels, particles, nanofibers, wafers, foams, and capsules that have found utility in numerous sectors such as food, pharmaceuticals, membranes, and cosmetics industries[1-3].

Based on its availability, biocompatibility, and lack of toxicity, alginate may be considered the most well-known polysaccharide derived from brown seaweed. Alginate is an anionic linear chain biopolymer composed of mannuronate sequence and guluronate residues in a variety of ratios, which, consequently, influences its molecular weight and physical properties[4-6]. Alginate solutions have the unique ability to crosslink fast in the presence of ions (such as Ca^{2+}), which produces a cohesive hydrogel with adjustable mechanical properties as function of alginate, crosslinker concentrations, and incremental timing.

Alginate is frequently utilized in additive manufacturing[6-8]. However, there are some overcoming issues due to the relatively low viscosity of alginate solutions which require arduous protocol adjustment to be able to print it in its purest form and crosslink it thereafter. To improve the immediate additive manufacturing, several approaches were used to overcome its limitations, including pre-crosslinking[9,10], rapid crosslinking during the printing process[6], and blending with other biopolymers[11]. Alginate, when combined with other biomaterials, gives the scaffold intrinsic biocompatibility, low toxicity, and moderate and controllable gelation with added divalent cations which are crucial for the encapsulation of cells or bioactive compounds. In this respect, alginate was compounded with gelatin[12-14], chitosan[15,16], methyl cellulose, or agarose[17-20] for obtaining proper hydrogel formulations that are used to create three-dimensional (3D) scaffolds with enhanced mechanical properties.

Therefore, according to recent reports, hydrogels fabricated based on the combination of two or more different polymers via crosslinkers can tackle disadvantages and integrate advantages. However, the mechanical properties of the hydrogels with multiple polymer networks are still weak and cannot fully meet the requirements of 3D printing. Consequently, the development of high-strength composite hydrogels becomes an emerging topic in hard tissue regeneration. In this respect, several composite formulations synthesized through the encapsulation or modifications of alginate-based hydrogels with additives, such as inert or bioactive glasses[21,22], hydroxyapatite[5,16], or nanoclays[23-26], have been explored.

In this context, our present work proposes a combined strategy where, for the first time, alginate networks will be semi-interpenetrated with salecan to obtain printable hydrogel formulations and further crosslinked 3D-printed alginate–salecan constructs. Salecan, which is a microbial marine polysaccharide extracted with a tolerant salt strain *Agrobacterium* sp. ZX09, demonstrated exceptional physical–chemical features[27]. Among excellent characteristics of salecan, its rheological properties[28-30] and availability to be used alongside natural[31-33] or synthetic polymers[34-36] are highly beneficial for our present study. In recent years, our research group developed polymer nanocomposites containing salecan for drug delivery purposes[37,38]. More recently, we have followed the possibility to synthesize solely salecan green crosslinked materials, and further, we have investigated using salecan for the first time in additive manufacturing[39].

On the other hand, nanoclays, which are categorized as either active components or excipients, are widely employed in medicine and pharmaceuticals, particularly for drug delivery purposes[38,40,41]. Clay nanoparticles have a strongly negatively-charged surface that is counterbalanced by positive metal counterions. Nanoclays consist of layered particles that are around 2 microns in diameter and 10 nm thick[42]. Many research studies proved that the mechanical properties of the generated polymer–clay composites, swelling and degradation of the materials, and drug encapsulation and/or release are all significantly modified by the addition of nanoclays into the polymeric materials because clay platelets influence the synthesis process[40,41,43-45]. In addition, clay nanoparticles were demonstrated to exhibit shear thinning properties to their corresponding nanocomposite hydrogels. Therefore, nanoclays are used in tissue engineering to produce 3D scaffolds using additive manufacturing technique. The presence of nanoclays also promoted osteogenesis and cell growth in the generated 3D-printed structures[24-26].

3D printing techniques for hydrogels offer numerous advantages in biomedical applications, such as customization, complex geometry, and spatial control[46-48]. The principal techniques used for 3D printing are as follows:

(i) Extrusion-based 3D printing: This technique involves the deposition of hydrogel filaments through a fine nozzle. It offers versatility in terms

of material selection and allows the incorporation of cells, drugs, and growth factors into the hydrogel matrix. Extrusion-based printing offers a high printing speed and is compatible with various hydrogel formulations[48-50].

(ii) Stereolithography: Stereolithography utilizes a liquid resin that solidifies upon exposure to light. This technique enables high-resolution printing and precise control over the structure. Stereolithography offers excellent spatial resolution and the ability to fabricate complex geometries. However, it is limited by the availability of suitable photopolymerizable hydrogels[46,47].

(iii) Inkjet printing: Inkjet printing deposits tiny droplets of hydrogel ink onto a substrate in a layer-by-layer manner. It is a versatile technique that allows precise control over the droplet size and placement. Inkjet printing enables the creation of heterogeneous hydrogel structures and is well-suited for fabricating tissue scaffolds. Nevertheless, it often suffers from low printing speed and limited viscosity and compatibility of material[47,51].

However, limitations include material availability and properties, resolution constraints, and post-processing requirements. The choice of hydrogel material impacts not only mechanical strength but also cell viability if these are included in the printing ink as in the case of bioprinting[49,51,52]. Achieving high resolution with hydrogels is challenging, and additional steps are needed for stability and functionality. Despite challenges, 3D printing of hydrogels holds promise for biomedical devices, tissue engineering, and drug delivery. Ongoing research aims to overcome limitations and expand applications in regenerative medicine and personalized healthcare.

Considering all these aspects, our present study follows the development of novel 3D-printable nanocomposite formulations using alginate–salecan-based hydrogel ink loaded with nanoclay. By manipulating the alginate–salecan weight fraction, and also the nanofiller amount, we could fabricate various nanocomposite inks to render 3D structures with high printing fidelity and enhanced porosity through a simple strategy. Our study carefully examined, in terms of physicochemical parameters, how salecan and nanoclay affected the properties of the printing formulations and the final crosslinked hydrogel nanocomposites. In this regard, hydrogel inks' rheological characteristics were followed as these are essential in the 3D printing process. Scanning electron microscopy, thermogravimetric, Fourier transform infrared, and X-ray diffraction (XRD) analyses were used to investigate the morphological as well as the structure of the obtained composite hydrogels. The crosslinked hydrogels' swelling capacity, pH sensitivity, and their mechanical stability in wet condition were thoroughly assessed. Moreover, preliminary biological investigations were pursued.

To the best of our knowledge, this work is the first methodical research on the assessment of alginate, salecan, and natural clay for 3D printing. The present research findings lead us to believe that the disclosed nanocomposite materials' design and the default 3D-printed structures will have a significant influence on the creation of unique advanced materials for specialized regenerative therapies.

2. Materials and methods

2.1. Materials

Alginic acid sodium salt and calcium chloride were acquired from Sigma-Aldrich, Norway. Salecan (>90% purity), which is an β-1,3 glucan with an average molecular weight of 2,000,000 g/mol, was purchased from Suzhou Health Chemicals Co., Ltd. (Suzhou, China). The nanoclay powder (natural montmorillonite, Cloisite Na) from Southern Clay Products Inc. (Gonzales, TX, USA) was used. Sulfuric acid (95%–97% purity) was purchased from Supelco (Darmstadt, Germany) while phenol (min. 99.5% purity) from Chimreactiv SRL (Bucharest, Romania). Buffer solutions of pH = 2, 5.5, and 7.4 were prepared in our laboratory using deionized water, 0.1 M hydrochloric acid (HCl, SC Chimreactiv SRL, Bucharest, Romania), and phosphate-buffered saline (PBS; pH = 7.4) tablets (137 mM sodium chloride, 2.7 mM potassium chloride, and 10 mM phosphate buffer; VWR Chemicals, Ohio, USA).

2.2. Preparation of the crosslinked polysaccharide samples

The following steps were taken to obtain the crosslinked polysaccharides samples: Powders of salecan and alginate were measured and thoroughly combined in the solid state. The resulted solid blend was poured over the specified amount of bi-distilled water and was mixed very well with a spatula. The samples were kept at 37°C until the next day and stirred mechanically with a spatula from time to time. The obtained homogenous hydrogels were then used in 3D printing process.

In the case of hydrogel-clay samples, firstly, the required amount of clay was added to the bi-distilled water. Then, the clay aqueous dispersion was magnetically mixed for 2 h at 350 rpm and ultrasonically processed for 5 min at 30% amplitude (in an ice bath). The dry solid mixture of alginate and salecan was then added. Further, the process was carried out in accordance with the steps that had already been mentioned.

2.3. 3D printing of hydrogel inks

The hydrogel-based inks were printed using the 3D Bioprinter 3D Discovery TM (RegenHU Ltd., Switzerland, Villaz-St-Pierre). The printing process was conducted using a direct dispensing print-head and a 5-mL syringe with an attached cylindrical nozzle, under varying printing pressures and speeds at room temperature. The generated 3D structures were crosslinked following the printing process by their submersion in a 2%wt. $CaCl_2$ solution for an hour. Crosslinked 3D structures were then washed thoroughly with distilled water and were subsequently freeze-dried. Acquired dried samples were stored in a desiccator at room temperature.

2.4. Determinations of gel fraction and the evaluation of salecan stability for the alginate–salecan-based hydrogel samples

The determination of biopolymers gel fraction was performed as follows: each 3D-printed sample was weighed and was introduced in 20 mL of deionized water for 24 h in distilled water at 40°C. In this way, all the uncrosslinked biopolymers were dissolved, and we were able to determine the sol part. The extracted hydrogel samples were freeze-dried and weighed again. Equation I was used to measure the samples gel fractions:

$$\% \text{ Gel fraction}= Mf \times 100/Mi \qquad (I)$$

where Mf = final weight of the freeze-dried construct and Mi = initial weight of the construct.

The stability of salecan chains entangled in alginate networks was evaluated by using the phenol sulfuric acid method[36,39]. Thus, the content of salecan in the washing solutions resulted from the extraction process and was evaluated by UV-VIS measurements, as previously described[39]. The amount of salecan which remained well entangled in the alginate networks was then determined. For the samples including inorganic partner, only the biopolymeric content was taken into account in calculating the gel fraction as well as for the evaluation of interpenetrated salecan.

2.5. Swelling and degradation analyses

The hydrogel-based 3D-printed dry samples were weighed and submerged in solutions with different pH (pH = 2, 5.5, and 7.4). Readings of the swollen samples weight were taken at each hydrogel's equilibrium time. This experiment was performed in duplicate. Swelling degree was calculated using Equation II:

$$\%ESD = (m_{\text{equilibrium swollen sample}} - m_{\text{dry sample}}) \times 100/m_{\text{dry sample}} \qquad (II)$$

where ESD is equilibrium swelling degree, and m is the weight of the sample in each case.

The degradation behavior of each sample was evaluated by immersing the specimens in water or PBS. The hydrogels were kept at 37°C for up to 7 days. The weight of equilibrium swollen samples was considered the initial weight. The hydrogel degradation degree was computed as the weight drop (w–w0) relative to the weight of the equilibrium swollen samples (w0). The measurements were performed in triplicate.

2.6. Morphological and structural analyses

Fourier transform infrared (FTIR) spectroscopy was used to structurally characterize the samples containing alginate, salecan, and nanoclay. The analyses were carried out using a Bruker Vertex 70 FTIR spectrometer (Bruker, Billerica, MA, USA). FTIR spectra in the 4000–400 cm^{-1} wavenumber region were captured.

Environmental scanning electron microscopy (ESEM-FEI Quanta 200, Eindhoven, The Netherlands) was employed to analyze the morphology of the printed lyophilized samples and their 3D structures, without being sputter-coated.

Computer microtomography analysis was performed using Bruker µCT 1272 high-resolution equipment. The samples were fixed on a support and scanned during a 180° rotation, with an image pixel size of 5 µm (one pixel depicting 5×5 µm from the physical sample), at 70 kV, 130 µA, 500 ms exposure time and at a rotation step of 0.25°. Scanning was performed without filter, and each 2D projection was the average of five consecutive frames. Each dataset contained 1080 2D projections (2×1640 pixels) which were further used in NRecon software to generate the 3D tomograms. All quantitative measurements were performed in CTAn software, on the reconstructed tomograms.

X-ray diffractometer (Rigaku Ultima IV, Tokyo, Japan) was used to ascertain the structure of the nanocomposite samples. At 40 kV and 30 mA, Cu Kα radiation (λ=1.5406 Å) was employed. Under air pressure and room temperature, all of the analyses were conducted on samples in powder form. The scanning speed was 1°/min, and the data collection interval was 2θ range 1–50°.

2.7. Rheological and mechanical analyses

A Kinexus Pro rheometer (Malvern) with plate–plate geometry (upper plate diameter = 20 mm) was employed to monitor the flow behavior of the synthesized materials. The gap between the two plates was maintained constant at 0.5 mm throughout the testing. The apparatus was equipped with Peltier element for precise temperature control and a stainless-steel hood to prevent dehydration during testing. To obtain information regarding the processability of the formulations, flow curves were registered in the shear rate interval of 10^{-3} to 10^3 at a working temperature of 25°C.

DMA Q800 TA Instruments (New Castle, DE, USA) was used to evaluate the mechanical behavior of the obtained 3D-printed hydrogel samples. Using a modified compression clamp, the cylindrical 3D-printed samples with ~12 mm in diameter and ~3 mm in thickness were employed for the analyses, which were carried out in dynamic frequency sweeps mode at 25°C to avoid the effects of water evaporation. Dynamic frequency sweeps were carried out over a frequency range of 0.1–5 Hz with a constant strain of 0.1% (in the linear viscoelastic area) to record the storage (G') and loss (G") moduli of the swollen 3D-printed samples. To confirm reproducibility, frequency tests were conducted three times, and the G' and G" were plotted against frequency. The frequency sweep modulus was analyzed using TA Universal Analysis.

Nanoindentation tests were performed using a TI Premier System (Hysitron Inc., Minneapolis, MN, USA) equipped with a three-side pyramidal Berkovich tip (total angles of 142.35° and radius of curvature of 150 nm). A normal load of 100 μN was applied using the trapezoidal load function (5 s loading, 2 s hold, 5 s unloading) to determine the values of reduced modulus (E), calculated using the Oliver–Pharr method.

2.8. Preliminary biological studies

Human dermal fibroblasts were used to test biocompatibility of the 3D-printed biomaterials. Cells were cultured in Dulbecco's Modified Eagle Medium with 10% fetal bovine serum at a density of 10^5 cells per well. For 24 h, the 3D structures were placed on top of the cells after being UV-sterilized. Following the manufacturer's instructions, cytotoxicity was assessed using the LDH (lactate dehydrogenase) Cytotoxicity kit (Sigma). With the use of a NanoQuant Infinite M200 Pro equipment, absorbance was measured at 490 nm. Utilizing the Live/Dead test (cat. no. L3224), the viability of the cells was evaluated. Using a Zeiss fluorescent microscope, imaging was done at λ = 494/517 (living cells) and λ = 517/617 (dead cells). Cell proliferation was quantified using the CyQUANT™ MTT (3-[4,5-dimethylthiazol-2-yl]-2,5 diphenyl tetrazolium bromide) Cell Viability Assay (thermos Scientific) in accordance with the manufacturer recommendations.

2.9. Statistical analyses

The data are expressed as mean and standard deviation. To evaluate the significance of differences, one-way analysis of variance (ANOVA) was performed. The significance was assessed if the p value was less than 0.05.

3. Results and discussion

Our present study investigated in the first step the possibility to obtain alginate–salecan hydrogels. In an effort to achieve improved fidelity and stability, different weight fractions of alginate and salecan were investigated and their inks were used in additive manufacturing. These bi-component hydrogels were further doped with different concentrations of clay nanoparticles and then used to print 3D nanocomposite structures. The resulted polysaccharides-based 3D constructions were further submerged in a $CaCl_2$ bath to allow alginate – COO^- functional groups to react with Ca^{2+} ions. Alginate networks became intertwined with salecan chains, creating semi-interpenetrating networks which were stabilized through physical interactions by alginate ionic crosslinking and also H–bonding interactions.

A schematic representation of the crosslinking mechanism of alginate–salecan networks in the presence of clay nanofiller is proposed in Scheme 1.

3.1. 3D printing of polysaccharide-based hydrogel inks

To reach the main goal of this research, i.e., obtaining appropriate inks for printing 3D constructs with excellent fidelity and stability, eight formulations were investigated. The 3D printing process was carried out at room temperature, employing the 3D printer's extrusion dispenser. Different types of needles (plastic or metallic with a diameter of 0.41 mm), printing pressures ranging from 150 to 620 kPa, and speeds ranging from 4 to 12 mm/s were examined as a function of ink composition as presented in Table 1.

Initially, the alginate hydrogel was prepared after tests involving 3D printing were performed on it. The low viscosity of the ink caused instability throughout the printing process; also, the layers collapsed as they came into contact with the glass slides, and the printed shape displayed apparent distortion due to the weight of the added layers.

In order to improve the rheological properties of the weak alginate hydrogel and to obtain 3D-printed constructs with improved shape fidelity, salecan was added as a second biopolymer network. Thus, three compositions of salecan and alginate in different weight ratios were created: salecan-alginate 1.687:3.620 (AV1), 2.653:2.653 (AV2), and 3.62:1.687 (AV3). 3D printing tests were performed using speeds in the range of 4–10 mm/s and pressures in the range of 180–500 kPa. The results showed that raising the salecan concentration enhanced the ink stability during the printing process when compared with neat alginate ink, and the resulted 3D-printed platforms maintained greater fidelity of up to seven layers (Figure 1).

Based on the 3D printing behavior cumulated with the results obtained from salecan retention in the alginate
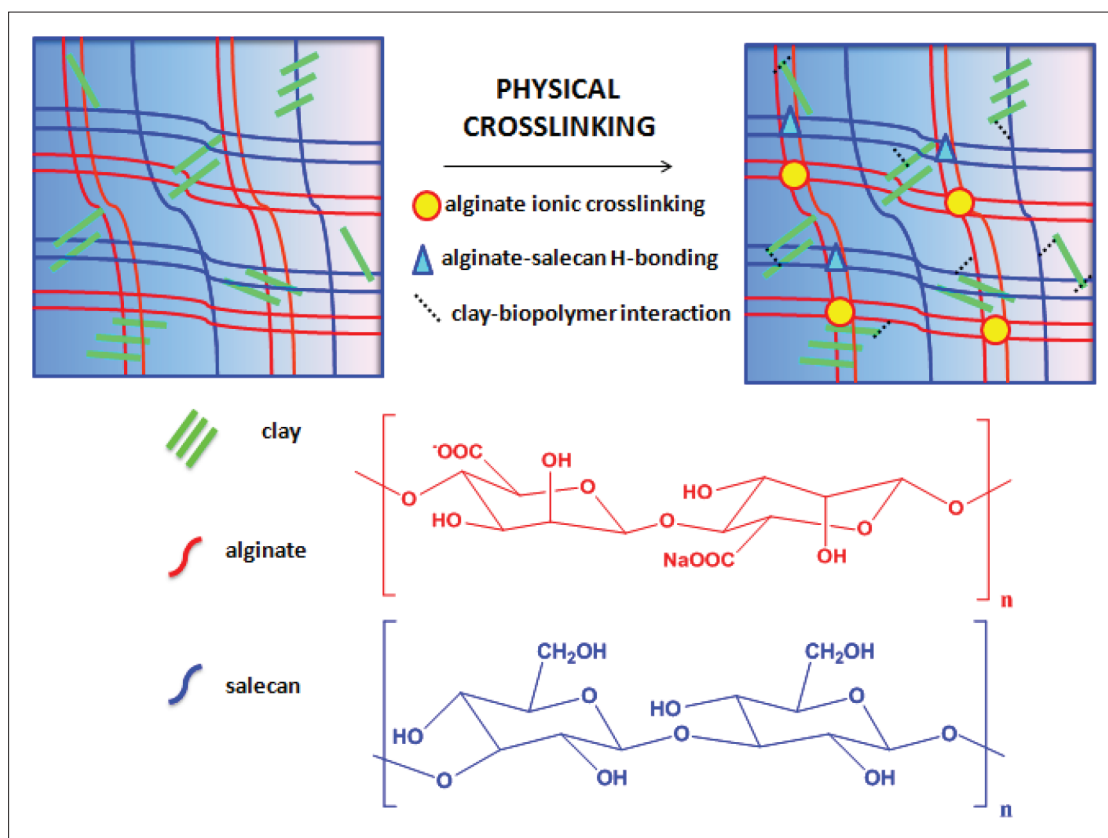
Scheme 1. Schematic representation of the crosslinked alginate–salecan-based semi-interpenetrating hydrogel nanocomposites.

Table 1. The annotation of the 3D printing formulations and their compositions

Sample	Alginate (g)	Salecan (g)	Water (g)	Clay (g)
AA0	3.620	-	30.054	-
AV1	3.620	1.687		-
AV2	2.653	2.653		-
AV3	1.687	3.62		-
AV2C1	2.653	2.653		1.060
AV2C2	2.653	2.653		1.767
AV2C3	2.653	2.653		2.474
AV2C4	2.653	2.653		3.535

matrix (presented in subsection 2.4), AV2 formulation was selected to be used in the further development of novel nanocomposite inks. Consequently, four concentrations of clay were varied (~3%, 5%, 7%, and 10%wt. with respect to the total mass of the hydrogel) in the AV2 alginate–salecan bi-component hydrogel yielding AV2C1, AV2C2, AV2C3, and AV2C4 formulations. The nanocomposites formulations were prepared and subjected to 3D printing process.

Different 3D shapes with varying heights were formed depending on the number of deposited layers, particularly circular shapes with a diameter of ~1.5 cm and square ones with a side of ~1 cm (Table 2). When compared to alginate–salecan printing inks, the nanocomposites inks demonstrated improved stability during the additive manufacturing process, and their default 3D-printed constructs retained better integrity of up to 10 layers (AV2C1), 15 layers (AV2C2), more than 30 layers (AV2C3), and more than 40 layers (AV2C4). 3D constructs based on ink called AV2C3 and AV2C4 preserved their 3D design best, as can be seen from the 3D printing images (Table 2) as well as the SEM images (Figure 4).

One thing worth taking into account was the fact that, even if the speed is limited to 4–8 mm/s, at higher clay concentrations, when the inks become highly viscous, the layers do not easily attach to each other. This caused previously deposited layers to be dragged, resulting in irregularly shaped 3D-printed structures (Figure 4, SEM images on rounded shape).

As a result, the printing process must be tuned beginning with the size of the needle, printing speed, printed shape, and number of layers in order to obtain regular forms with high fidelity and integrity. Based on our observation of the printing process, the utilization of ~7%–10% clay-loaded
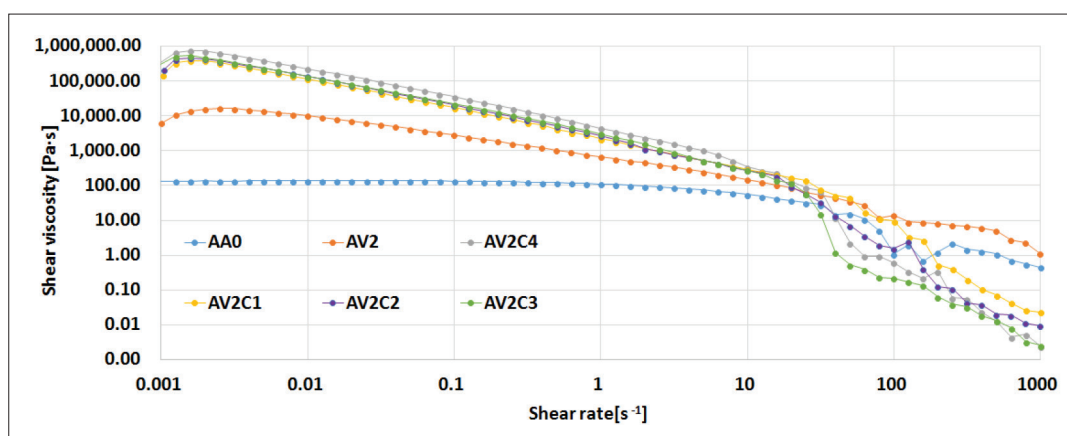
Figure 1. Shear rate as function of shear viscosity for the prepared hydrogel inks.

alginate–salecan nanocomposite hydrogels stands out as the most promising nanocomposite printing inks.

3.2. Rheology studies of the polysaccharide-based Hydrogels

Rheological characterization of materials provides a general overview of the system's viscoelastic flow characteristics. For the most effective 3D printing of paste or viscous solutions, an understanding of ink rheology is required. For 3D printing of inks, shear thinning and high yield strength are essential rheology qualities to take into account.

As shown in Figure 1, all hydrogels displayed a shear thinning characteristic during the examined shear rates interval. Thus, shear rate as function of shear viscosity revealed that alginate ink exhibits an extended Newtonian plateau followed by a gradual decrease of viscosity at shear rates above 10 s^{-1}. This behavior indicated a slow rearrangement of the macromolecular chains.

The rest of the alginate–salecan-based compositions presented a shear thinning behavior in the studied shear rate interval. The presence of inorganic partner in the polysaccharide hydrogel was correlated with an increase in viscosity. This rheological characteristic, which is typical for composite hydrogels, was related to the interaction of clay nanoplatelets with polymer chains, which resulted in high viscosities and pseudoplasticity. Moreover, the composite hydrogel inks presented a sudden viscosity drop around 25 s^{-1}. This phenomenon can be attributed to a reorganization of the internal structure of the macromolecules or breakage of physical bonds formed between clay layers and macromonomers. Additionally, the shear thinning behavior indicated the feasibility of injecting the composite hydrogel-based inks as their viscosity dropped and the shear rate increased.
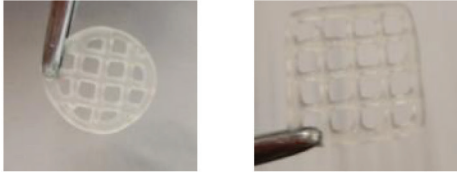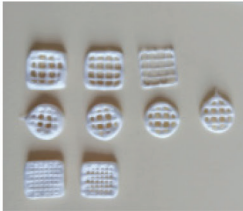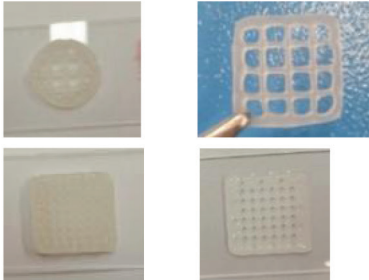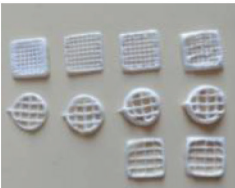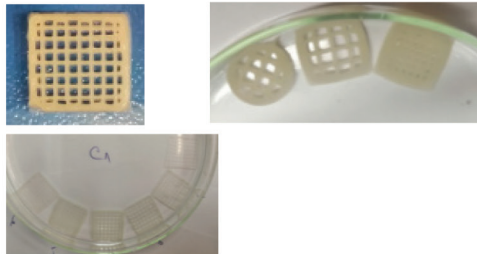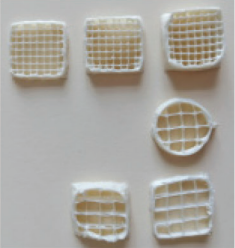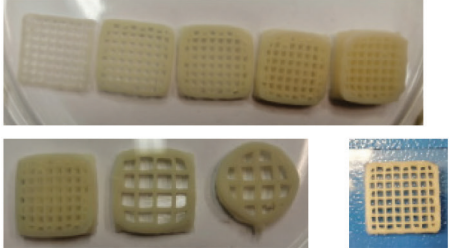
To preserve the shape of extruded items, the rheology of the ink must be properly adapted. In light of the fact that

hydrogel viscosity reduced with increasing shear rate in pressure-regulated flows, the use of the prepared composite ink formulations with shear thinning behavior is optimal. Based on the rheology analyses, we could assume that the 3D-printed material's overall structure should be preserved, and the yield strength should be high enough to withstand the weight of the post-extruded ink. Although hydrogels are the most often employed forms of viscous materials in extrusion type 3D printing, these inks typically have very low viscosities and stiffness. Reformulation in the form of bi-component hydrogels or hydrogels that include an inorganic partner, as described also in our research paper, is encouraged in order to achieve the appropriate ink rheology[24,25,53].

3.3. Assessment of biopolymer network stability and determination of gel fraction for the 3D-printed crosslinked constructs

The stability of salecan chains entangled in alginate crosslinked networks was identified by measuring the amount of salecan in the washing solutions of the 3D-printed structures. The results of the phenol sulfuric acid approach presented in Table 3 revealed that the alginate network effectively captured the majority of the salecan biopolymer. However, when a larger quantity of salecan was used in the synthesis phase, the experiments indicated the release of a larger amount of biopolymer in the washing solution, from 10% for AV1 to 40% for AV3 sample. Based on these data as well as observations from the printing stage of the hydrogels, AV2 sample was chosen as having the suitable characteristics for further dosing with clay nanoparticles. When 3D nanocomposites were tested, it was possible to see that the calculated amount of salecan that was released into the washing fluid was lower when the probes included higher clay concentrations. This phenomenon could be explained by two physical interactions: first, the potential hydrogen bonds formed between the hydroxyl groups of salecan and the clay

Table 2. 3D printing parameters and the appearance of the resulted 3D constructs

Sample	Pressure (kPa)	Speed (mm/s)	Number of layers	Freeze-dried 3D-printed samples	3D-printed hydrogel samples
AA0	560	6–8	2–5		
AV1	130	4–8, 12	2–5		
AV2	150	4–8	5–7		
AV3	180	8–10	5–7		
AV2C1	225–300	4–8	10		
AV2C2	220–330	4–6	15		

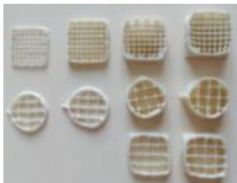(*Continued*)

Table 2. *Continued*
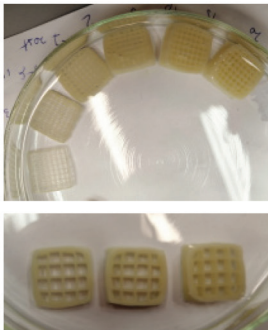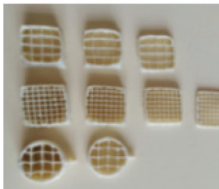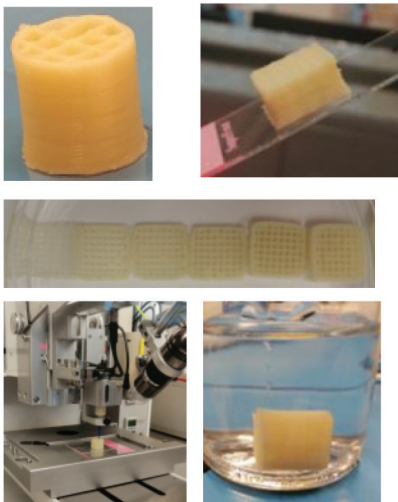
Sample	Pressure (kPa)	Speed (mm/s)	Number of layers	Freeze-dried 3D-printed samples	3D-printed hydrogel samples
AV2C3	300–481	6–8	30		
AV2C4	550–620	4–6	40		

Table 3. Results from UV and gel fraction investigations

Sample	Retained salecan (%)	Gel fraction (%)
AA0	0	86
AV1	97	80
AV2	89	76
AV3	60	53
AV2C1	90	71
AV2C2	93	78
AV2C3	95	79
AV2C4	96	80

structure, and second, the physical barrier created by clay platelets positioned within the polymeric matrix, which limited salecan detachment[38,43,54].

The gel fraction percentage in the absence of salecan was determined to be 86%, indicating that the alginate networks were almost entirely crosslinked. At varied salecan doses inside the alginate matrix, the gel fraction dropped to less than 53%–80%. This behavior can be attributed to the addition of salecan to alginate hydrogel, which may suppress the formation of crosslinked alginate chains and, as a result, greatly slow down the gelation process. In the case of nanocomposite samples, as clay nanoparticles content rose, composite hydrogel gel fractions slightly increased. Thus, nomadic polysaccharides were probably hindered by the presence of clay nanoparticles as observed from the determination of salecan content. These findings are consistent with earlier studies that showed that nanoclay platelets can function as a barrier in an eluting agent's path[40,41,54]. A strategy useful in drug delivery applications should be conceived. Thus, a bioactive agent may be added to this nanocomposite hydrogel system, and the amount of salecan or clay partner inside an alginate matrix may be optimized to adjust the drug's release.

3.4. Swelling behavior of the 3D-printed constructs
Swelling analyses in media of different pH could provide useful information when attempting to obtain
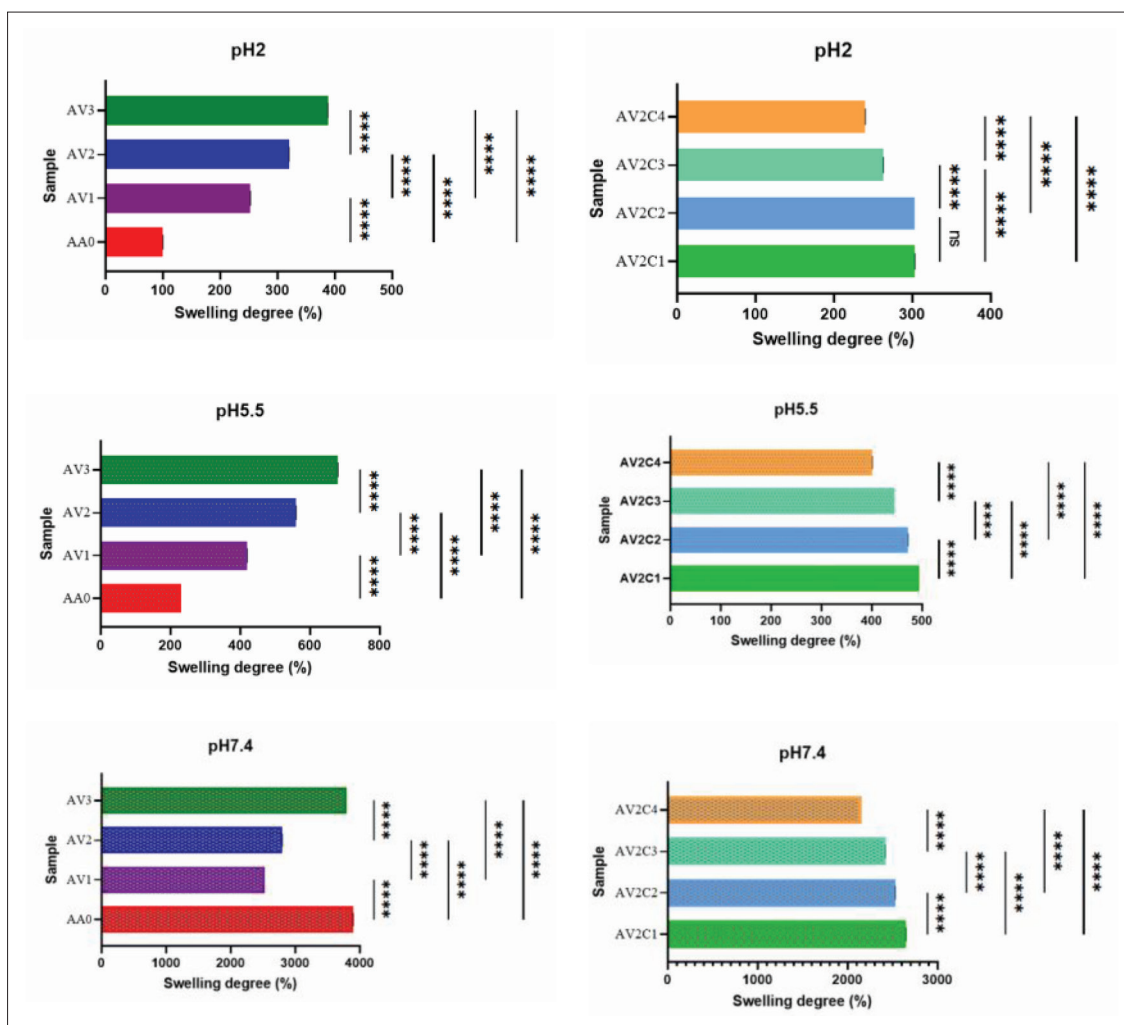
Figure 2. Swelling behavior of the 3D-printed constructs in aqueous environments of different pH. $**p < 0.005$; $****p < 0.0001$.

pH-dependent materials for applications that require proper stability at the targeted site or, depending on the circumstance, pH-dependent drug release or even controlled dissolvability/degradation. In this regard, the pH sensitivity of the novel polysaccharide materials was investigated by incubating the 3D-printed constructs in a variety of pH environments (pH = 2, 5.5, and 7.4) and calculating the equilibrium swelling degree. The results obtained for each polysaccharide-based hydrogels are presented in Figure 2.

Alginate and salecan are two examples of macromolecular polymers having COOH and OH functional groups, respectively, which affect the level of swelling of the resultant materials depending on different pH conditions. At pH < 7, the presence of an excess of H$^+$ ions facilitates the protonation of functional groups and increase the likelihood of intermolecular hydrogen bonding with water molecules[55]. Accordingly,

water molecules are either hindered or accommodated in the macromolecular semi-interpenetrating network depending on pH of media. The resulting nanocomposites materials are further complicated by the presence of anionic clay that also contains OH groups. On the other hand, the swelling behavior of the 3D-printed constructions might be influenced by the porosity of the obtained hydrogels. As the CT studies showed, clay quantity as well as salecan and clay addition improved the samples' porosity. In our situation, the phenomenon of fluid retention is more likely to be caused by the makeup of the samples than by their increased porosity.

The samples displayed the least swelling at acidic pHs, when compared to neutral pH, most likely because of multiple hydrogen bonds that tighten the biopolymer networks and hinder water molecule from penetrating. The degree of swelling and subsequent disintegration increased as the pH rose because the groups began to

ionize, the electrostatic repulsive forces between system components increased, and the fluids were encouraged to enter into the semi-interpenetrating biopolymer-based network[39,44].

Depending on the pH, the analyzed samples reach constant weight in different times. Thus, the maximum degree of swelling occurs at pH = 2 in about 6 h, while for experiments conducted at higher pH levels, the swelling degree reached its maximum in about 48 h and 72 h for pH 5.5 and 7.4, respectively. On the other hand, samples maintained in media at neutral pH swell enormously and disintegrate after 72 h, producing relatively loose hydrogel structures that were unable to be weighed. Samples held in deionized water (pH = 5.5) retained their shape for a longer period of time. After around 3 weeks, the 3D constructs began to disintegrate. The nanocomposite samples disintegrated in a percentage of ~80–90%wt. as opposed to the pristine polysaccharide samples, which retain their shape in a proportion of ~95%wt. Herein, we assume that the increased porosity in the presence of clay (revealed further through CT analyses) enhances the scaffold's contact surface with the incubation medium and boosts the degradability of the samples, as stated by other research groups[56].

The hydrogel's ability to swell is significantly influenced by both the matrix composition and its surface hydrophilicity. When salecan biopolymer was added to the alginate matrix, the 3D polysaccharide constructs had varying degrees of hydrophilicity. Thus, at low pH, the ESD increased in the presence of salecan and as the amount of salecan in the biopolymeric matrix was greater. These findings, supported also by salecan retention tests, demonstrated that higher alginate concentrations resulted in more crosslinking sites, which in turn produced a more restricted semi-interpenetrating network. Consequently, larger amounts of salecan resulted in a decrease in network packing and higher ESD. Moreover, salecan structure which is rich in OH groups favored increased fluid retention at higher concentrations[27,32].

When compared to the associated biopolymeric matrix, all nanocomposite samples presented ESD changes. In each case, adding clay to the alginate–salecan matrix as well as the increasing clay concentration reduced the swelling's intensity. It is quite likely that this behavior is related to the chemical composition of the resulting nanocomposites, given that clay was added to the system and did not retain as much water as the substituted polysaccharide. Furthermore, the physical interactions between the biopolymer and the clay, involving hydrogen bonds, as well as the increase in matrix crystallinity, as revealed by XRD studies, could result in lesser molecular flexibility

and may restrict hydrogel swelling, as confirmed by other researchers[25,40,55,57].

In summary, according to swelling data, the novel alginate–salecan-based 3D constructs exhibited pH sensitivity and adjustable swelling degree achieved with modification of the nanocomposite system's constituent parts. These findings may enable the development of useful materials with a variety of operating pHs, depending on the foreseen application.

The samples' degradation was assessed by incubating the specimens in distilled water or PBS at 37°C for 7 days. After this period, it was found that all the samples stored in water degraded with a loss of ~3%wt. The samples retained their inflated shape extremely well, being particularly stable at pH of 5.5. On the other hand, the composite samples with high silicate content (AV2C3 and AV2C4) kept in PBS began to disintegrate, with little pieces detaching from the sample. After 5 days, the samples completely degraded and appeared as discrete delaminated layers in the PBS. In contrast, the samples with minimal silicate content (AV2C1 and AV2C2), as well as the non-compounded biopolymeric sample AV2, are well maintained in PBS and do not degrade over the 7-day study more than ~10%wt. As previously noted by other researchers, this behavior could be related to the increased level of clay dispersion and intercalation within biopolymeric matrix at low clay content[58,59]. Another point worth noticing is that round-shaped samples retained their shape better than square-shaped samples, which is most likely owing to the more compact structure.

In summary, all samples incubated in water are stable for up to 7 days, but only samples with low silicate content are highly stable in PBS, and the high content of inorganic partner leads to full deterioration of the 3D-printed constructs. These findings could be useful for tailoring the degradation of a material in a certain environment based on the planned application.

3.5. Mechanical behavior of the 3D-printed constructs

As substrates for tissue regeneration and repair, 3D hydrogel-based constructs are of great interest because of their tissue-like composition with linked porosity and the potential for tailored fabrication. The generally poor mechanical strength of 3D hydrogel-printed materials is a typical drawback, limiting their utility in various clinical applications. In this regard, in our study, we developed composite inks that outperform hydrogels made solely from alginate or alginate–salecan, in terms of final mechanical quality and structural integrity of the 3D-printed structures.
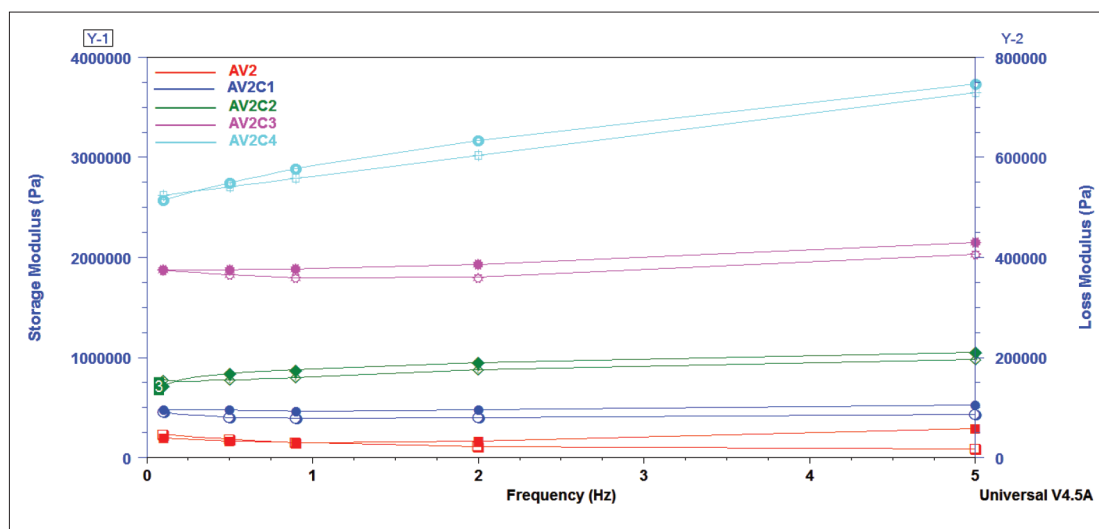
Figure 3. Storage modulus (G') and loss modulus (G") as a function of frequency for the crosslinked 3D-printed hydrogel-based samples.

The storage (G') and loss (G") moduli, registered for the crosslinked 3D hydrogel-based structures, are shown in Figure 3 as a function of frequency. The moduli of the equilibrium swollen samples were determined using the frequency sweep method. It is essential to note that for all the samples under investigation, G' is higher than G" over the whole frequency range of 0.1 to 5 Hz, attesting the crosslinked condition of the resulting 3D structures. Additionally, the addition of clay nanoparticles and the rise in their concentration in the formulations used for 3D printing resulted in an increase in the storage modulus G' and loss modulus G", respectively. This event suggested that clay nanoparticle interfered in the crosslinking mechanism and 3D-printed composite hydrogels were becoming more rigid and able to tolerate higher mechanical stress.

The acquired results are consistent with prior research investigations that demonstrate the creation of more stiff biomaterials by combining biopolymeric networks or adding inorganic components. Thus, Serafin *et al.* showed that the mechanical characteristics are noticeably improved when collagen is combined with gelatin or hyaluronic acid[60]. The same group found that the storage modulus increases as the amount of inorganic partner increases in the collagen–gelatin matrix. Furthermore, as the frequency was raised, both moduli—storage and loss—increased as well. The hydrogels continue to exhibit an elastic response as a result, and the storage modulus continues to be greater than the loss modulus[61]. Other studies have demonstrated also how the addition of clay to polymeric matrices had a favorable impact on the rheological and mechanical properties of the produced nanocomposites[57,62].

The reduced moduli/elastic moduli were determined from nanoindentation results using the Oliver–Pharr method. The addition of clay nanoparticles increased the elastic moduli, showing that the nanocomposites were stiffer than the neat biopolymer sample (AV2). Thus, the elastic moduli values for the synthesized alginate–salecan nanocomposite materials were 7.28×10^3 for AV2C1, 12.06×10^3 KPa for AV2C2, 11.39×10^3 KPa for AV2C3, and 7.34×10^3 KPa for AV2C4, all of which were greater than the elastic modulus of the uncompounded alginate–salecan sample (AV2, 5.21×10^3 KPa). These values are comparable to the elastic moduli of soft tissues (brain, skin, and muscles)[63-66]. The nanoparticles are likely to impede the movement of the biopolymer networks, according to the findings, which are consistent with earlier research on polymer–clay nanocomposites[40,44,67]. Following that, the samples with the highest clay concentration showed a little decline, demonstrating that an optimal clay content (of ~5 and 7%wt.) is required to achieve larger elastic moduli. This effect could be explained by the dispersion of nanoclay particles within the alginate–salecan matrix, which is more pronounced with low clay concentrations, as indicated by XRD analyses, as well as the remodeling of the internal structure under applied mechanical stress[40,55].

In summary, the nanocomposite samples demonstrated augmented mechanical stability compared with the neat biopolymer sample, which is critical when the material is projected for applications that are subjected to mechanical stress.

3.6. Microscopy analyses

SEM analyses of freeze-dried 3D structures were also carried out to investigate their morphology when created with various compositions. The macrostructure underwent visible changes as a result of the viscosity of the probe as observed from SEM images presented in Figure 4. Thus,
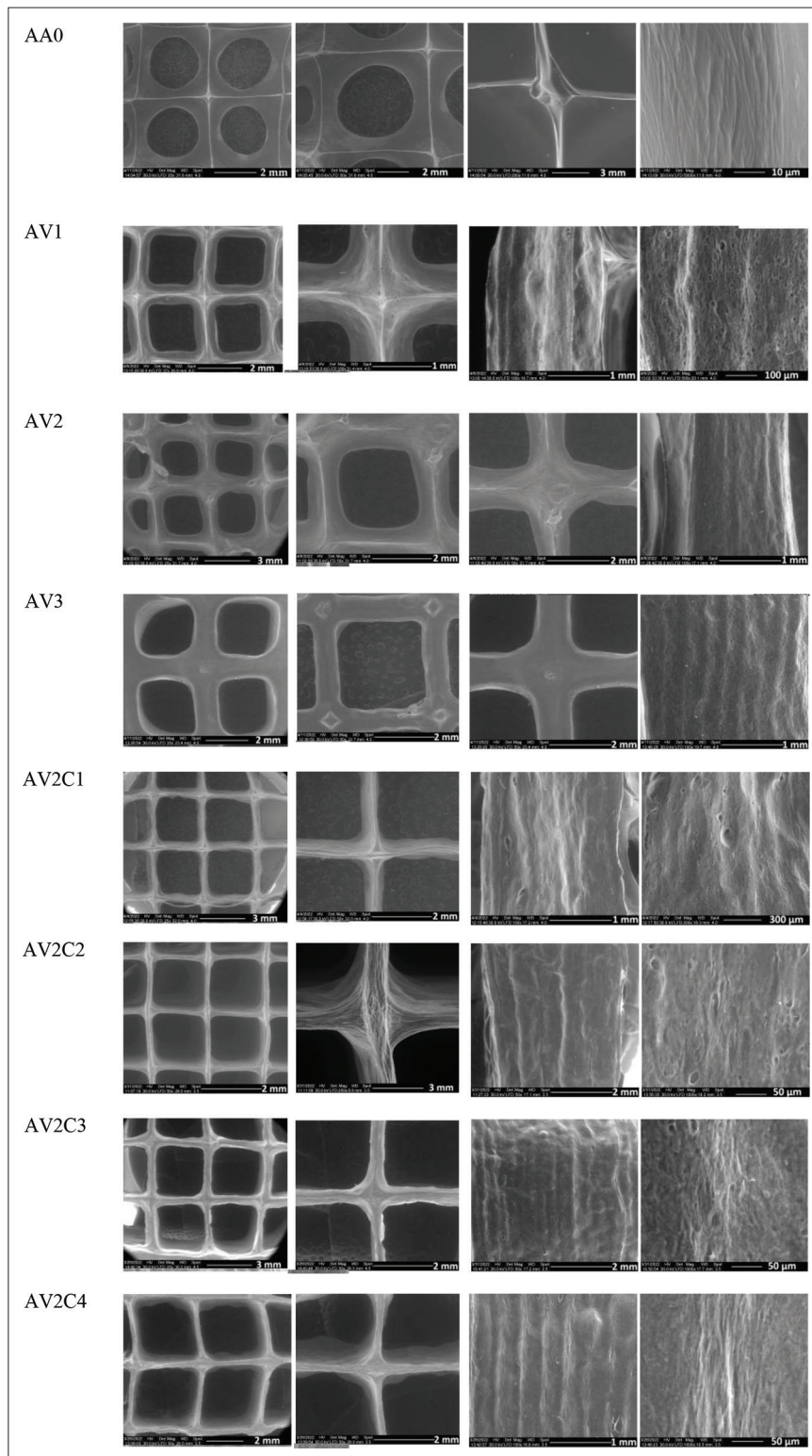
Figure 4. SEM images of the 3D constructs open macropores, filaments crossroads, and outer surface.

with higher concentrations of salecan, and further clay, the pores macrostructure is better defined as a result of increased viscosities and consequently, printing stability as compared to probes with lower concentrations of salecan, without clay or with low clay concentrations. As a result, as the ink formulations were less viscous, the 3D-printed constructs began to collapse under the weight of the printed layers.

The surface observed when examining the 3D structures was relatively smooth. With the addition of clay, there was a change in the surface morphology, specifically, some roughness caused by clay particulate agglomeration in the composition. These became more visible when the concentration of clay in the hydrogel matrix was increased. The most noticeable feature of SEM images is that printed probes had distinct filaments, which were more visible at higher concentrations of salecan as well as clay in the hydrogel ink. Furthermore, the filaments in the layered samples attached very effectively to one another.

Taken together, by modifying the concentration of salecan and nanoclay in the original biopolymer sample, the morphology of the 3D constructions can be tailored to obtain 3D constructs with enhanced printing fidelity and structure stability.

3.7. Structural analyses, FTIR and XRD

The results of FTIR spectrophotometric analyses presented in Figure 5 have shown the characteristic peaks for alginate and salecan as well as changes or shifts of these specific peaks depending on the composition of the materials. Sodium alginate presented the following commonly known wavelengths: ~1017 cm^{-1} for the C-O-C and C-OH bonds, ~1600 cm^{-1} for asymmetrical stretching vibration of COO$^-$ group, ~1420 cm^{-1} for symmetrical COO$^-$ group stretching vibration, and ~2900 cm^{-1} for CH symmetric stretching vibration[57]. In the case of the alginate–salecan sample investigation, the FTIR curves revealed a slightly modified peak spanning around 1019 cm^{-1}, which was attributed to alginate–salecan chain interactions considering that salecan generally exhibits the characteristic C-OH absorption band corresponding to the glucopyranose ring from the polysaccharide structure in the mentioned area[39,68,69].

FTIR tests on nanocomposites based on alginate and salecan confirmed the presence of biopolymer-specific peaks along with the specific peaks of the clay, namely, vibrations of Si-O-Si at ~1000 cm^{-1}, Al-Si-O at 450–620 cm^{-1}, and OH in the range of 3400–3600 cm^{-1}[57,62,70]. However, certain changes in the shape of the FTIR curve may be seen between 1007 and 1020 cm^{-1}, especially the presence of a sharper peak with a minor shift from the assigned

polysaccharide or clay peaks. These modifications may be explained by the overlapping of the component's peaks and also the possible interactions between the various groups of the components (COOH and OH groups from alginate, OH groups from salecan, and OH from clay edges), as shown in previous studies[38,44,70]. Thus, FTIR analyses confirmed that the structural changes of alginate–salecan biopolymer matrix occurred after clay inclusion with interactions between components and slight peak shifts depending on clay concentration.

X-ray diffraction analyses presented in Figure 6 also indicated changes in the structure of the semi-interpenetrated biopolymeric matrices as well as of their nanocomposites. XRD curve of the AA0 pristine alginate sample revealed by the existence of two diffraction peaks at 2θ ~13° and ~ 22°, respectively. These weak and broad peaks are generally ascribed to a rather amorphous structure of alginate[71]. The bi-component samples also showed a typical salecan peak-of-diffraction at 20°, which rose with increasing microbial polysaccharide content. As a result, the X-ray curves revealed a partly crystalline structure with a dominating amorphous phase, which was ascribed to hydrogen-bonding interactions between polysaccharides COOH and OH functional groups on alginate and salecan polysaccharides. These results were consistent with FTIR findings which demonstrated biopolymeric chains interactions, too. Furthermore, prior investigations in which salecan polysaccharide was mixed with other natural polymers, such as agarose, chitosan, κ-carrageenan, and xanthan gum, also revealed modifications in the resulted biopolymer matrices[33,72-74].

The existence of the specific peak of nanoclay around 2θ ~4–7° was confirmed in the XRD profile of polysaccharide-based nanocomposites. This peak underwent some changes in intensity and width, indicating an advanced dispersal of clay platelets in biopolymer matrix, mostly at low clay concentrations. Changes in inter-basal distance may suggest biopolymer molecules insertion between silicate lamella and the formation of mainly intercalated structures, a fact strongly related with the rheological behavior of the nanocomposites inks. Moreover, the findings are in accordance with prior research that demonstrated that adding nanoclay particles to polymeric systems increases the matrix's crystallinity, which in turn has an impact on the swelling phenomena[55].

3.8. Evaluation of the internal morphology of the 3D-printed object by computed tomography

Computed tomography (CT) analysis was performed in order to depict the internal morphology of the 3D-printed object and to investigate whether the chemical composition
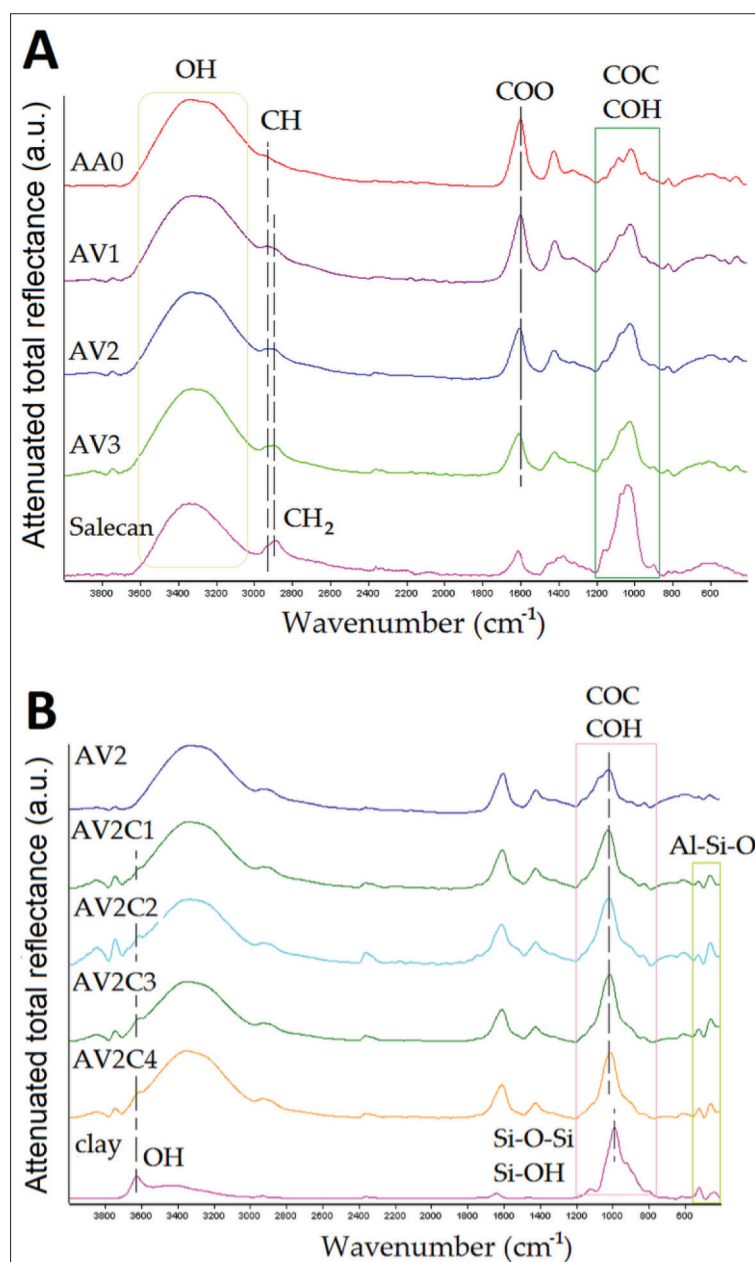
Figure 5. FTIR spectra of the crosslinked biopolymer-based samples: (A) alginate–salecan samples and (B) alginate–salecan composites samples.

variation influenced the architecture. Moreover, considering the scanning resolution (image pixel size = 5 μm), some quantitative characteristics were extracted from the tomograms, listed in Table 4—the surface of the object, porosity, as well as the average wall thickness and pore diameter.

Their exhaustive distribution per size domains is plotted in the charts of Figure 7 for samples AA0 to AV2C1. Printed sample morphology differs with the amount of inorganic phase they contain. The composition also has an impact on the pore patterning during freeze-

drying process; the pristine AA0 sample exhibited a thin but compact morphology, with a reduced pore/solid matter ratio. On the other hand, AV2 is characterized by a more common morphology for objects fabricated via lyophilization. Starting with sample AV2C1, the pores and shape of the deposited filaments showed drastic changes. Probably because of the increasing amount of reinforcing agent, more physical interactions were formed between the two phases of the composite and the filaments tended to maintain their original shape and CAD model fidelity. Another reason for that might be linked to the increase of
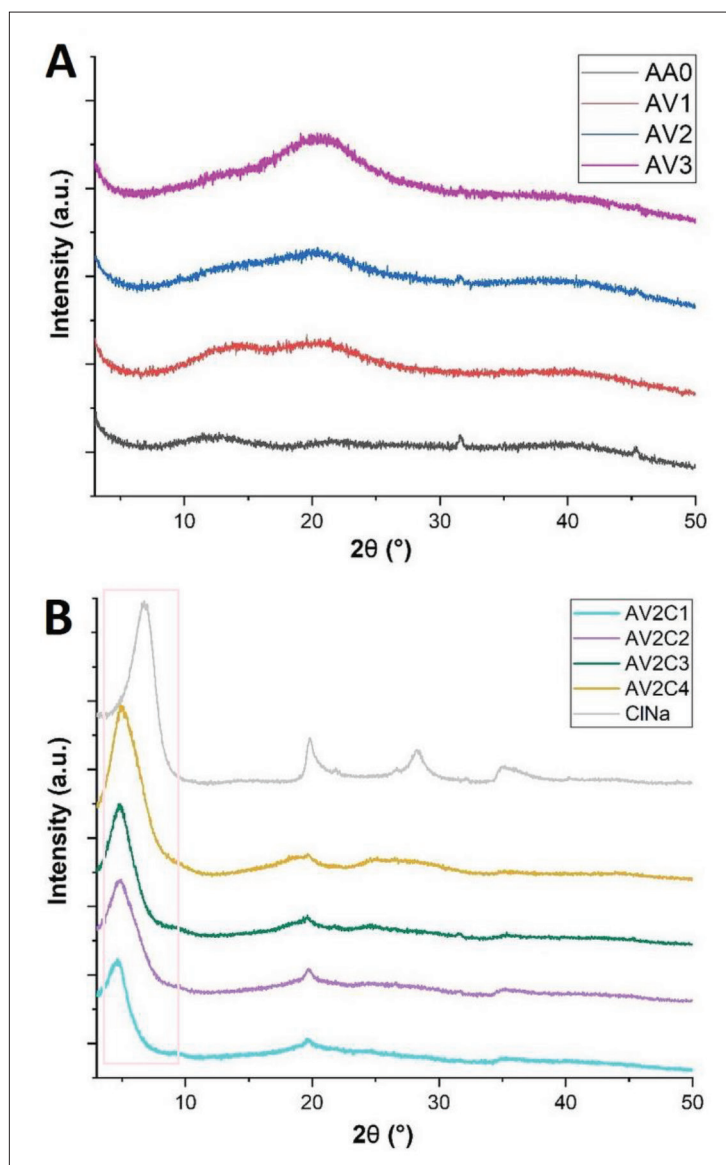
Figure 6. X-ray diffraction curves for the polysaccharide based-samples: (A) alginate–salecan samples and (B) alginate–salecan nanocomposites samples.

viscosity of the inks which favored the shape preservation and limited the spilling effect after extrusion.

The objects fabricated with composite inks feature complex pore network with easily discernible particularities. First of all, the walls in the control sample exceed 100 μm, but the object has a very low porosity overall (< 5%); however, the composite formulations were patterned in templates consisting of structures of up to 120 μm, yet, to a lower extent. Even though the share of thicker walls was generally low, these kinds of assemblies could significantly improve the mechanical behavior of the ensemble. Also, with the exception of AA0, the distribution of wall thickness domains was a left-skewed Gaussian bell, with a maximum

incidence of 20 ± 5 μm. Conversely, the pore domain distributions depicted only the inner porosity from the filaments and excluded the large pores that were built-in from the beginning in the 3D CAD model. Pore template was impacted to a higher extent than wall structuration. From samples AA0 to AV2C4, the distribution of pore domains and the total porosity (in the filaments) increased steadily, going beyond the threshold of 200 μm and a share of 71.5% porosity in sample AV2C4. This augmentation was favored by the addition of the inorganic phase and the interfaces between the dispersed agent and the polymer matrix; these submicronic disruptions favored the fusion of water crystals during the freezing process and enabled, eventually, the attainment of larger pores. In addition,

Table 4. Quantitative features measure in CTAn software of the control and composite prints

Sample	Object surface (µm²)	Porosity (%)		Medium wall thickness (µm)	Medium pore diameter (µm)
		Total	Closed		
AA0	7.96×10^8	4.99	2.05	69.1	26.5
AV2	8.37×10^9	36.0	3.13	37.1	27.2
AV2C1	3.25×10^9	53.3	0.30	30.3	42.3
AV2C2	5.49×10^9	57.9	0.12	39.6	56.2
AV2C3	7.58×10^9	63.8	0.08	28.7	58.2
AV2C4	10.2×10^{10}	71.5	0.05	47.8	94.5

the porosity was highly interconnected as the incidence of closed pores dropped to 0.05% of the total porosity in AV2C4 (Table 4).

Overall, compositing the alginate–salecan hydrogel formulations enhanced the pore ratio in the extruded filaments, decreased the incidence of close pores, increased the total surface of the solid object (exterior and inner pore surface included), and guided pore size distribution toward larger domains (Table 3). Besides, with the exception of AV2C3 sample, most walls thickened and their mean value increased by approximately 25%. The outcome of this architectural design adjustment could be in favor of the intended application of the 3D constructs since interconnectivity, solid surfaces, and large interface areas with the environment are essential prerequisites of favorable outcome in cell seeding and in-volume proliferation[75].

3.9. Preliminary biological studies

Cytotoxicity is one of the most important factors to consider when selecting materials for biomedical applications. Live/Dead, MTT, and LDH (lactate dehydrogenase) tests performed on human dermal fibroblasts were used to determine the effect of 3D structures on the viability of cells.

Human dermal fibroblasts were grown in 3D structures, and the cell viability of those cells was assessed using Live/Dead staining. A majority of the cells placed in the tested 3D-printed hydrogels were still alive after 2 and 6 days of incubation, as evidenced by the green fluorescence shown in Figure 8. Further evidence that these 3D-printed hydrogels are non-toxic to human dermal fibroblasts comes from LDH test, which revealed no statistically significant difference in the cytotoxicity results between the 3D structures and the negative control sample. The good biocompatibility of the new 3D-printed samples was additionally validated by MTT test.

The analyzed 3D structures showed excellent biocompatibility in the LDH, MTT, and Live/Dead assays,

indicating their potential use in biomedical applications. The results are consistent with other studies where clay-containing hydrogels displayed potential biological properties[42,73,76].

4. Conclusion

The present study's findings demonstrate the potential applications of alginate, salecan, and nanoclay for precise production of 3D hydrogel constructs using printing techniques. Ionic crosslinking and H-bonding between system partners influenced the morphostructure of the resulted composite hydrogels as revealed by FTIR and XRD analyses with consequences on salecan retention in the alginate network and the resulted materials gel fraction. Rheological and mechanical investigation indicated enhanced qualities, which was promoted by various physical interactions, following the increase in clay concentration.

Additionally, the hydrogels' composition governed both their degradation and swelling behavior in various pH conditions.

The features of the composite inks as well as the 3D-printed structures, where the pore shape preserved the 3D architecture better after printing, were significantly influenced by the use of clay at high concentrations of ~7%wt. and 10%wt. The addition of the second biopolymeric network as well as clay in the bi-component hydrogel matrix, particularly with increased clay concentration, increased the porosity, according to morphological assessments.

The novel bionanomaterials presented in the current work are recommended for application in regenerative medicine attributed to their exquisite porosity structure, connected pore-network surface topology, improved mechanical characteristics, and biocompatibility. Future studies will focus on the incorporation of bioactive substances into 3D-printed objects and the analysis of drug release in response to environmental factors.
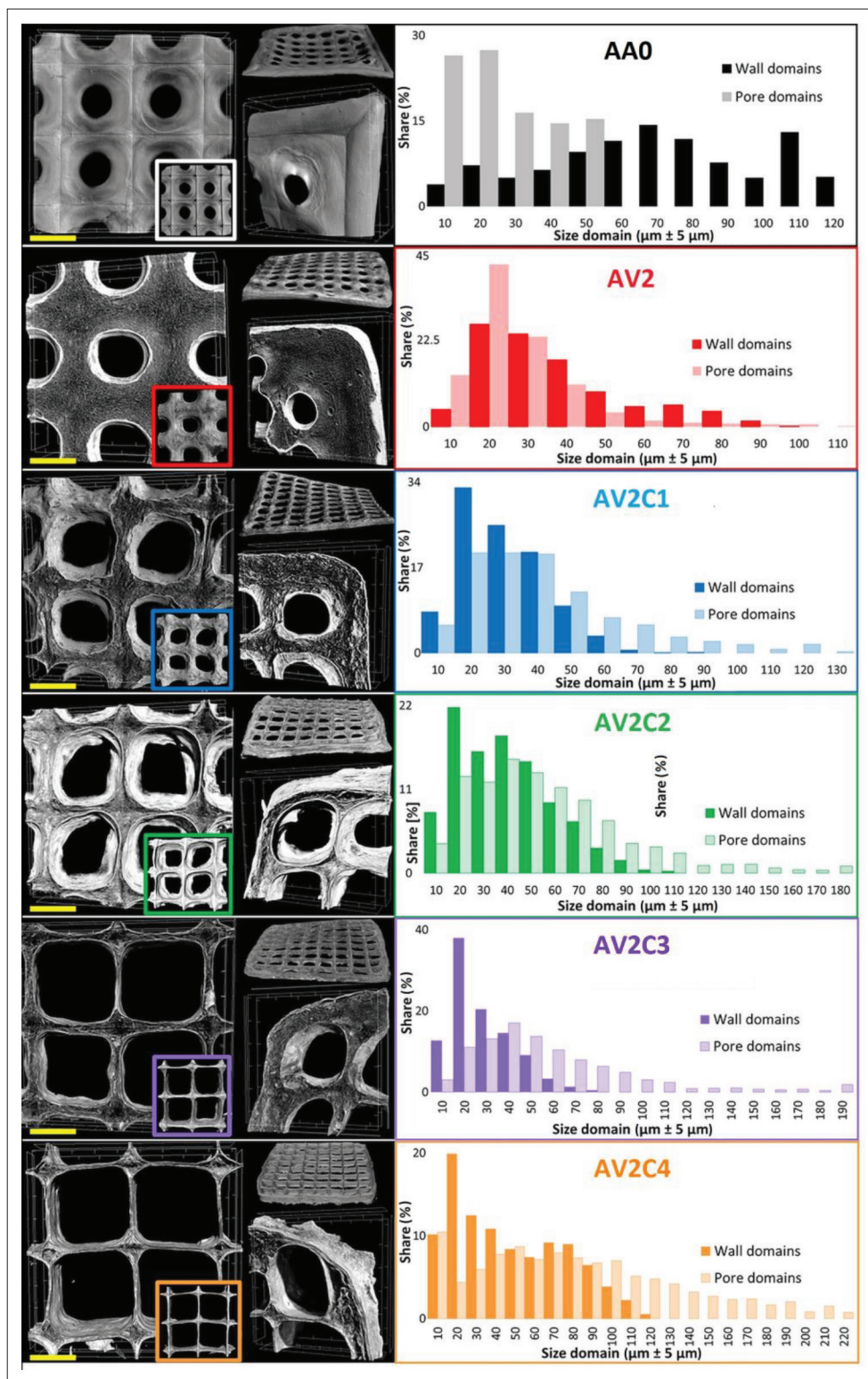
Figure 7. Computed tomography images of the 3D-printed specimens depicting cross-sectional views, superficial feature, and entire sample. The distance between two pins of the 3D box corresponds to 5 to 500 µm; yellow scale bar represents 1 mm. The bar charts depict the data of wall thickness and pore size distribution measured in CTAn.
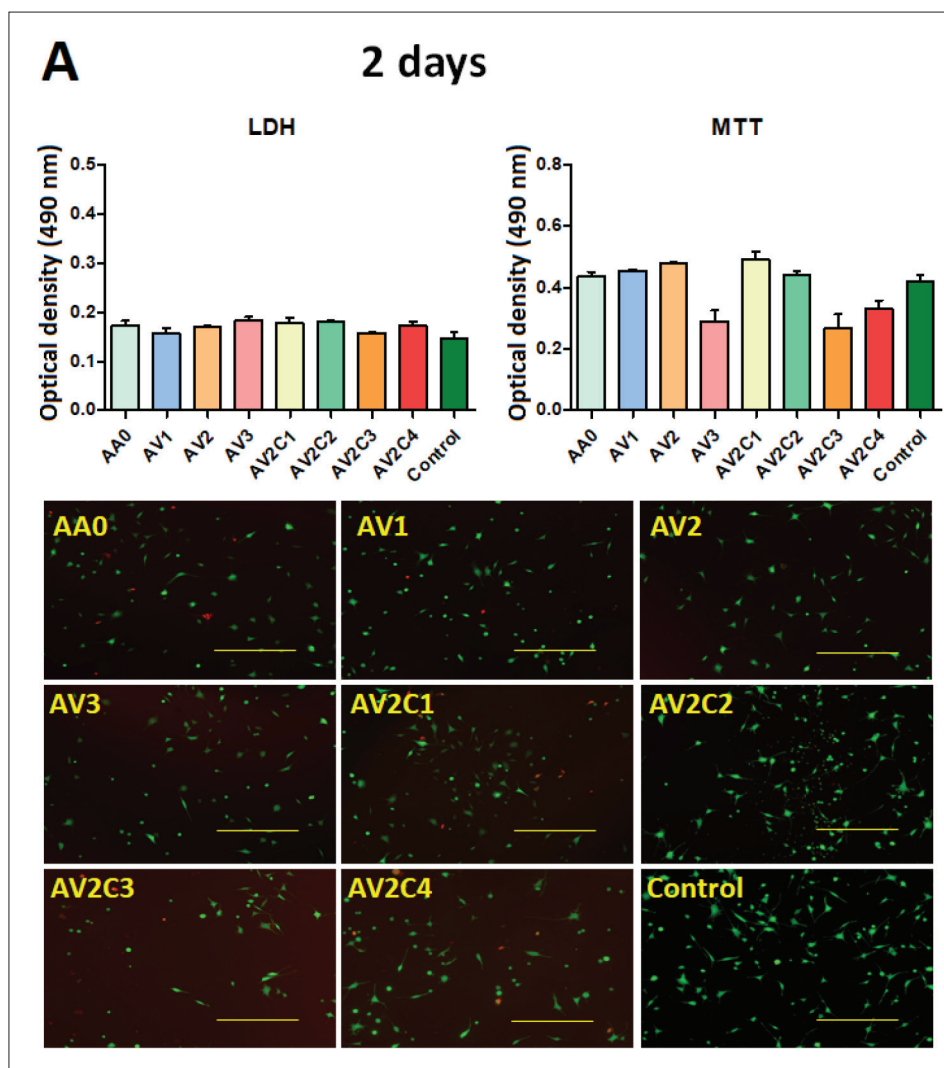
Figure 8. Results of preliminary biological studies based on MTT, LDH, and Live/Dead tests at (A) 2 days and (B) 6 days. Scale bar: 800 μm.

Acknowledgments

Funding

Conflict of interest

The authors declare no conflict of interest.

Author contributions

Conceptualization: Raluca Ianchis, Maria Minodora Marin, Rebeca Leu Alexa

Formal analysis: Raluca Ianchis, Ioana Catalina Gifu, Maria Minodora Marin, Elvira Alexandrescu, George Mihail Vlasceanu, Andrada Serafim, Cristina Lavinia Nistor Gratiela Gradisteanu Pircalabioru, George Mihail Teodorescu, Silviu Preda

Investigation: Raluca Ianchis, Ioana Catalina Gifu, Maria Minodora Marin, Elvira Alexandrescu, George Mihail Vlasceanu, Andrada Serafim, Cristina Lavinia Nistor, Gratiela Gradisteanu Pircalabioru, George Mihail Teodorescu, Silviu Preda

Supervision: Raluca Ianchis, Cristian Petcu

Writing – original draft: Raluca Ianchis, Maria Minodora Marin, Rebeca Leu Alexa, Ioana Catalina Gifu, George Mihail Vlasceanu, Cristina Lavinia Nistor

Writing – review & editing: Raluca Ianchis, Maria Minodora Marin, Rebeca Leu Alexa, Ioana Catalina Gifu, George Mihail Vlasceanu, Cristina Lavinia Nistor, Gratiela Gradisteanu Pircalabioru

All authors have read and agreed to the published version of the manuscript.

Ethics approval and consent to participate

Not applicable.

Consent for publication

Not applicable.

Availability of data

Data will be provided by corresponding author on request.

References

1. Mohammed ASA, Naveed M, Jost N, 2021, Polysaccharides; classification, chemical properties, and future perspective applications in fields of pharmacology and biological medicine (a review of current applications and upcoming potentialities). *J Polym Environ*, 29(8): 2359–2371.

   https://doi.org/10.1007/s10924-021-02052-2

2. Zhang X, Kim G, Kang M, *et al.*, 2018, Marine biomaterial-based bioinks for generating 3D printed tissue constructs. *Marine Drugs*, 16(12): 484.

   https://doi.org/10.3390/md16120484

3. Sharma A, Kaur I, Dheer D, *et al.*, 2023, A propitious role of marine sourced polysaccharides: Drug delivery and biomedical applications. *Carbohydr Polym,* 308: 120448.

   https://doi.org/10.1016/j.carbpol.2022.120448

4. Aderibigbe B, Buyana B, 2018, Alginate in wound dressings. *Pharmaceutics*, 10(2): 42.

   https://doi.org/10.3390/pharmaceutics10020042

5. Ahmad Raus R, Wan Nawawi WMF, Nasaruddin RR, 2021, Alginate and alginate composites for biomedical applications. *Asian J Pharm Sci*, 16(3): 280–306.

   https://doi.org/10.1016/j.ajps.2020.10.001

6. Datta S, Barua R, Das J, 2020, Importance of alginate bioink for 3D bioprinting in tissue engineering and regenerative medicine, in *Alginates - Recent Uses of This Natural Polymer*, IntechOpen, UK.

   https://doi.org/10.5772/intechopen.90426

7. Axpe E, Oyen M, 2016, Applications of alginate-based bioinks in 3D bioprinting. *IJMS*, 17(12): 1976.

   https://doi.org/10.3390/ijms17121976

8. Mallakpour S, Azadi E, Hussain CM, 2021, State-of-the-art of 3D printing technology of alginate-based hydrogels—An emerging technique for industrial applications. *Adv Colloid Interface Sci,* 293: 102436.

   https://doi.org/10.1016/j.cis.2021.102436

9. Hazur J, Detsch R, Karakaya E, *et al.*, 2020, Improving alginate printability for biofabrication: Establishment of a universal and homogeneous pre-crosslinking technique. *Biofabrication*, 12(4): 045004.

   https://doi.org/10.1088/1758-5090/ab98e5

10. Falcone G, Mazzei P, Piccolo A, *et al.*, 2022, Advanced printable hydrogels from pre-crosslinked alginate as a new tool in semi solid extrusion 3D printing process. *Carbohydr Polym,* 276: 118746.

    https://doi.org/10.1016/j.carbpol.2021.118746

11. Piras CC, Smith DK, 2020, Multicomponent polysaccharide alginate-based bioinks. *J Mater Chem B*, 8(36): 8171–8188.

    https://doi.org/10.1039/D0TB01005G

12. Distler T, Solisito AA, Schneidereit D, *et al.*, 2020, 3D printed oxidized alginate-gelatin bioink provides guidance for C2C12 muscle precursor cell orientation and differentiation via shear stress during bioprinting. *Biofabrication*, 12(4): 045005.

    https://doi.org/10.1088/1758-5090/ab98e4

13. Amr M, Dykes I, Counts M, *et al.*, 2021, 3D printed, mechanically tunable, composite sodium alginate, gelatin and Gum Arabic (SA-GEL-GA) scaffolds. *Bioprinting*, 22: e00133.

    https://doi.org/10.1016/j.bprint.2021.e00133

14. Alruwaili M, Lopez JA, McCarthy K, *et al.*, 2019, Liquid-phase 3D bioprinting of gelatin alginate hydrogels: Influence of printing parameters on hydrogel line width and layer height. *Bio-des Manuf*, 2(3): 172–180.

    https://doi.org/10.1007/s42242-019-00043-w

15. Huang J, Fu H, Wang Z, *et al.*, 2016, BMSCs-laden gelatin/sodium alginate/carboxymethyl chitosan hydrogel for 3D bioprinting. *RSC Adv*, 6(110): 108423–108430.

https://doi.org/10.1039/C6RA24231F

16. Sadeghianmaryan A, Naghieh S, Yazdanpanah Z, *et al.*, 2022, Fabrication of chitosan/alginate/hydroxyapatite hybrid scaffolds using 3D printing and impregnating techniques for potential cartilage regeneration. *Int J Biol Macromol,* 204: 62–75.

https://doi.org/10.1016/j.ijbiomac.2022.01.201

17. Li H, Tan YJ, Leong KF, *et al.*, 2017, 3D bioprinting of highly thixotropic alginate/methylcellulose hydrogel with strong interface bonding. *ACS Appl Mater Interfaces*, 9(23): 20086–20097.

https://doi.org/10.1021/acsami.7b04216

18. Kanafi NM, Rahman NA, Rosdi NH, 2019, Citric acid cross-linking of highly porous carboxymethyl cellulose/poly(ethylene oxide) composite hydrogel films for controlled release applications. *Mater Today: Proc,* 7(Part 2): 721–731.

https://doi.org/10.1016/j.matpr.2018.12.067

19. Aljohani W, Ullah MW, Li W, *et al.*, 2018, Three-dimensional printing of alginate-gelatin-agar scaffolds using free-form motor assisted microsyringe extrusion system. *J Polym Res*, 25(3): 62.

https://doi.org/10.1007/s10965-018-1455-0

20. Wang J, Liu Y, Zhang X, *et al.*, 2021, 3D printed agar/calcium alginate hydrogels with high shape fidelity and tailorable mechanical properties. *Polymer*, 214: 123238.

https://doi.org/10.1016/j.polymer.2020.123238

21. Bednarzig V, Schrüfer S, Schneider TC, *et al.*, 2022, Improved 3D printing and cell biology characterization of inorganic-filler containing alginate-based composites for bone regeneration: Particle shape and effective surface area are the dominant factors for printing performance. *Int J Mol Sci,* 23(9): 4750.

https://doi.org/10.3390/ijms23094750

22. Bider F, Karakaya E, Mohn D, Boccaccini AR, 2022, Advantages of nanoscale bioactive glass as inorganic filler in alginate hydrogels for drug delivery and biofabrication. *EJMS*, 2(1): 33–53.

https://www.tandfonline.com/doi/epdf/10.1080/26889277.2022.2039078?needAccess=true&role=button

23. Shahbazi M, Jäger H, Ahmadi SJ, *et al.*, 2020, Electron beam crosslinking of alginate/nanoclay ink to improve functional properties of 3D printed hydrogel for removing heavy metal ions. *Carbohydr Polym,* 240: 116211.

https://doi.org/10.1016/j.carbpol.2020.116211

24. Ahlfeld T, Cidonio G, Kilian D, *et al.*, 2017, Development of a clay based bioink for 3D cell printing for skeletal application. *Biofabrication*, 9(3): 034103.

https://doi.org/10.1088/1758-5090/aa7e96

25. Alexa RL, Iovu H, Trica B, *et al.*, 2021, Assessment of naturally sourced mineral clays for the 3D printing of biopolymer-based nanocomposite inks. *Nanomaterials*, 11(3): 703.

https://doi.org/10.3390/nano11030703

26. Cidonio G, Glinka M, Kim YH, *et al.*, 2020, Nanoclay-based 3D printed scaffolds promote vascular ingrowth *ex vivo* and generate bone mineral tissue *in vitro* and *in vivo*. *Biofabrication*, 12(3): 035010.

https://doi.org/10.1088/1758-5090/ab8753

27. Qi X, Wei W, Shen J, *et al.*, 2019, Salecan polysaccharide-based hydrogels and their applications: A review. *J Mater Chem B*, 7(16): 2577–2587.

https://doi.org/10.1039/C8TB03312A

28. Fu R, Li J, Zhang T, *et al.*, 2018, Salecan stabilizes the microstructure and improves the rheological performance of yogurt. *Food Hydrocoll,* 81: 474–480.

https://doi.org/10.1016/j.foodhyd.2018.03.034

29. Fan Z, Cheng P, Gao Y, *et al.*, 2022, Understanding the rheological properties of a novel composite salecan/gellan hydrogels, *Food Hydrocolloids*, 123: 107162

https://www.sciencedirect.com/science/article/pii/S0268005X21005786

30. Zhang Q, Ren T, Gan J, *et al.*, 2022, Synthesis and rheological characterization of a novel salecan hydrogel. *Pharmaceutics*, 14(7): 1492.

https://doi.org/10.3390/pharmaceutics14071492

31. Fan Z, Cheng P, Yin G, *et al.*, 2020, *In situ* forming oxidized salecan/gelatin injectable hydrogels for vancomycin delivery and 3D cell culture. *J Biomater Sci,* 31(6): 762–780.

https://doi.org/10.1080/09205063.2020.1717739

32. Gan J, Sun L, Guan C, *et al.*, 2022, Preparation and properties of salecan-soy protein isolate composite hydrogel induced by thermal treatment and transglutaminase. *Int J Mol Sci*, 23(16): 9383.

https://doi.org/10.3390/ijms23169383

33. Qi X, Su T, Tong X, *et al.*, 2019, Facile formation of salecan/agarose hydrogels with tunable structural properties for cell culture. *Carbohydr Polym*, 224: 115208.

https://doi.org/10.1016/j.carbpol.2019.115208

34. Hu X, Wang Y, Zhang L, *et al.*, 2017, Redox/pH dual stimuli-responsive degradable Salecan-g-SS-poly(IA-co-HEMA) hydrogel for release of doxorubicin. *Carbohydr Polym,* 155: 242–251.

https://doi.org/10.1016/j.carbpol.2016.08.077

35. Qi X, Wei W, Li J, *et al.*, 2017, Design of salecan-containing semi-IPN hydrogel for amoxicillin delivery. *Mater Sci Eng C*, 75: 487–494.

https://doi.org/10.1016/j.msec.2017.02.089

36. Wei W, Hu X, Qi X, *et al.*, 2015, A novel thermo-responsive hydrogel based on salecan and poly(N-isopropylacrylamide): Synthesis and characterization. *Colloids Surf B: Biointerfaces*, 125: 1–11.

https://doi.org/10.1016/j.colsurfb.2014.10.057

37. Munteanu T, Ninciuleanu CM, Gifu IC, *et al.*, 2018 The effect of clay type on the physicochemical properties of new hydrogel clay nanocomposites, IntechOpen, UK.

https://www.intechopen.com/chapters/59586

38. Florian PE, Icriverzi M, Ninciuleanu CM, *et al.*, 2020, Salecan-clay based polymer nanocomposites for chemotherapeutic drug delivery systems; characterization and in vitro biocompatibility studies. *Materials*, 13(23): 5389.

https://doi.org/10.3390/ma13235389

39. Ianchis R, Alexa RL, Gifu IC, *et al.*, 2023, Novel green crosslinked salecan hydrogels and preliminary investigation of their use in 3D printing. *Pharmaceutics*, 15(2): 373.

https://doi.org/10.3390/pharmaceutics15020373

40. Ianchis R, Ninciuleanu C, Gifu IC, *et al.*, 2018, Hydrogel-clay nanocomposites as carriers for controlled release. *CMC*, 25(6): 919–954.

https://doi.org/10.2174/0929867325666180831151055

41. Jafarbeglou M, Abdouss M, Shoushtari AM, *et al.*, 2016, Clay nanocomposites as engineered drug delivery systems. *RSC Adv*, 6(55): 50002–50016.

https://doi.org/10.1039/C6RA03942A

42. Marin MM, Ianchis R, Leu Alexa R, *et al.,* 2022, Development of new collagen/clay composite biomaterials. *Int J Mol Sci,* 23(1): 401.

https://doi.org/10.3390/ijms23010401

43. Gaharwar AK, Cross LM, Peak CW, *et al.*, 2019, 2D nanoclay for biomedical applications: regenerative medicine, therapeutic delivery, and additive manufacturing. *Adv Mater*, 31(23): 1900332.

https://doi.org/10.1002/adma.201900332

44. Ninciuleanu CM, Ianchiş R, Alexandrescu E, *et al.*, 2021, The effects of monomer, crosslinking agent, and filler concentrations on the viscoelastic and swelling properties of poly(methacrylic acid) hydrogels: A comparison. *Materials (Basel)*, 14(9): 2305.

https://doi.org/10.3390/ma14092305

45. Fialová L, Capek I, Ianchis R, *et al.,* 2008, Kinetics of styrene and butyl acrylate polymerization in anionic microemulsions in presence of layered silicates. *Polym J*, 40(2): 163–170.

https://doi.org/10.1295/polymj.PJ2007160

46. Fan D, Li Y, Wang X, *et al.*, 2020, Progressive 3D printing technology and its application in medical materials. *Front Pharmacol*, 11:122.

https://doi.org/10.3389/fphar.2020.00122

47. Ghilan A, Chiriac AP, Nita LE, *et al.*, 2020, Trends in 3D printing processes for biomedical field: Opportunities and challenges. *J Polym Environ*, 28(5): 1345–1367.

https://doi.org/10.1007/s10924-020-01722-x

48. Jiang T, Munguia-Lopez JG, Flores-Torres S, *et al.*, 2019, Extrusion bioprinting of soft materials: An emerging technique for biological model fabrication. *Appl Phys Rev,* 6(1): 011310.

https://doi.org/10.1063/1.5059393

49. Jiang Z, Diggle B, Tan ML, *et al.*, 2020, Extrusion 3D printing of polymeric materials with advanced properties. *Adv Sci*, 7(17): 2001379.

https://doi.org/10.1002/advs.202001379

50. Joas S, Tovar G, Celik O, *et al.*, 2018, Extrusion-based 3D printing of poly(ethylene glycol) diacrylate hydrogels containing positively and negatively charged groups. *Gels*, 4(3): 69.

https://doi.org/10.3390/gels4030069

51. Suntornnond R, Ng WL, Huang X, *et al.*, 2022, Improving printability of hydrogel-based bio-inks for thermal inkjet bioprinting applications via saponification and heat treatment processes. *J Mater Chem B*, 10(31): 5989–6000.

https://doi.org/10.1039/D2TB00442A

52. Ng WL, Lee JM, Zhou M, *et al.*, 2020, Vat polymerization-based bioprinting—process, materials, applications and regulatory challenges. *Biofabrication*, 12(2): 022001.

https://doi.org/10.1088/1758-5090/ab6034

53. Coppola B, Cappetti N, Di Maio L, *et al.*, 2018, 3D printing of PLA/clay nanocomposites: Influence of printing temperature on printed samples properties. *Materials*, 11(10): 1947.

https://doi.org/10.3390/ma11101947

54. Kianfar F, Dempster N, Gaskell E, *et al.*, 2017, Lyophilised biopolymer-clay hydrogels for drug delivery. *MJNDR*, 1(1): 1–9.

https://doi.org/10.18689/mjndr-1000101

55. Chaudhuri SD, Dey A, Upganlawar S, *et al.*, 2022, Influence of clay concentration on the absorption and rheological attributes of modified cellulose /acrylic acid based hydrogel and the application of such hydrogel. *Mater Chem Phys,* 282: 125942.

https://doi.org/10.1016/j.matchemphys.2022.125942

56. Kumar A, Won SY, Sood A, *et al.*, 2022, Triple-networked hybrid hydrogels reinforced with montmorillonite clay and graphene nanoplatelets for soft and hard tissue regeneration. *IJMS*, 23(22): 14158.

https://doi.org/10.3390/ijms232214158

57. Leu Alexa R, Ianchis R, Savu D, *et al.*, 2021, 3D printing of alginate-natural clay hydrogel-based nanocomposites. *Gels*, 7(4): 211.

https://doi.org/10.3390/gels7040211

58. Stloukal P, Pekařová S, Kalendova A, *et al.,* 2015, Kinetics and mechanism of the biodegradation of PLA/clay nanocomposites during thermophilic phase of composting process. *Waste Manag,* 42: 31–40.

https://doi.org/10.1016/j.wasman.2015.04.006

59. Pluta M, Paul MA, Alexandre M, *et al.,* 2006, Plasticized polylactide/clay nanocomposites. II. The effect of aging on structure and properties in relation to the filler content and the nature of its organo-modification. *J Polym Sci B Polym Phys*, 44(2): 312–325.

https://doi.org/10.1002/polb.20697

60. Serafin A, Culebras M, Collins MN, 2023, Synthesis and evaluation of alginate, gelatin, and hyaluronic acid hybrid hydrogels for tissue engineering applications. *Int J Biol Macromol,* 233: 123438.

https://doi.org/10.1016/j.ijbiomac.2023.123438

61. Serafin A, Murphy C, Rubio MC, *et al.,* 2021, Printable alginate/gelatin hydrogel reinforced with carbon nanofibers as electrically conductive scaffolds for tissue engineering. *Mater Sci Eng C*, 122: 111927.

https://doi.org/10.1016/j.msec.2021.111927

62. Dávila JL, d'Ávila MA, 2019, Rheological evaluation of Laponite/alginate inks for 3D extrusion-based printing. *Int J Adv Manuf Technol*, 101(1–4): 675–686.

https://doi.org/10.1007/s00170-018-2876-y

63. Hickey RJ, Pelling AE, 2019, Cellulose biomaterials for tissue engineering. *Front Bioeng Biotechnol*, 7: 45.

https://doi.org/10.3389/fbioe.2019.00045

64. Saveleva MS, Eftekhari K, Abalymov A, *et al.,* 2019, Hierarchy of hybrid materials—The place of inorganics-in-organics in it, their composition and applications. *Front Chem*, 7: 179.

https://doi.org/10.3389/fchem.2019.00179

65. Sachot N, Engel E, Castano O, 2014, Hybrid organic-inorganic scaffolding biomaterials for regenerative therapies. *COC*, 18(18): 2299–2314.

https://doi.org/10.2174/1385272819666140806200355

66. Handorf AM, Zhou Y, Halanski MA, *et al.,* 2015, Tissue stiffness dictates development, homeostasis, and disease progression. *Organogenesis*, 11(1): 1–15.

https://doi.org/10.1080/15476278.2015.1019687

67. Marin MM, Gifu IC, Pircalabioru GG, *et al.,* 2023, Microbial polysaccharide-based formulation with silica nanoparticles; A new hydrogel nanocomposite for 3D printing. *Gels*, 9(5): 425.

https://doi.org/10.3390/gels9050425

68. Hu X, Yan L, Wang Y, *et al.,* 2020, Microwave-assisted synthesis of nutgall tannic acid–based salecan polysaccharide hydrogel for tunable release of β-lactoglobulin. *Int J Biol Macromol,* 161: 1431–1439.

https://doi.org/10.1016/j.ijbiomac.2020.07.250

69. Hu X, Wang Y, Zhang L, *et al.,* 2018, Design of a pH-sensitive magnetic composite hydrogel based on salecan graft copolymer and Fe3O4@SiO2 nanoparticles as drug carrier. *Int J Biol Macromol,* 107: 1811–1820.

https://doi.org/10.1016/j.ijbiomac.2017.10.043

70. Mollah MZI, Faruque MRI, Bradley DA, *et al.,* 2023, FTIR and rheology study of alginate samples: Effect of radiation. *Radiat Phys Chem,* 202: 110500.

https://doi.org/10.1016/j.radphyschem.2022.110500

71. Zheng H, Yang J, Han S, 2016, The synthesis and characteristics of sodium alginate/graphene oxide composite films crosslinked with multivalent cations. *J Appl Polym Sci,* 133(27): 43616.

https://doi.org/10.1002/app.43616

72. Hu X, Yan L, Xu M, *et al.,* 2023, Photo-degradable salecan/ xanthan gum ionic gel induced by iron (III) coordination for organic dye decontamination. *Int J Biol Macromol,* 238:124132.

https://www.x-mol.com/paper/1638753777226412032

73. Qi X, Su T, Zhang M, *et al.,* 2020, Macroporous hydrogel scaffolds with tunable physicochemical properties for tissue engineering constructed using renewable polysaccharides. *ACS Appl Mater Interfaces*, 12(11): 13256–13264.

https://doi.org/10.1021/acsami.9b20794

74. Fan Z, Cheng P, Wang D, *et al.,* 2020, Design and investigation of salecan/chitosan hydrogel formulations with improved antibacterial performance and 3D cell culture function. *J Biomater Sci,* 31(17): 2268–2284.

https://doi.org/10.1080/09205063.2020.1800907

75. Foudazi R, Zowada R, Manas-Zloczower I, *et al.,* 2023, Porous hydrogels: Present challenges and future opportunities. *Langmuir*, 39(6): 2092–2111.

https://doi.org/10.1021/acs.langmuir.2c02253

76. Lee KY, Mooney DJ, 2012, Alginate: Properties and biomedical applications. *Prog Polym Sci,* 37(1): 106–126.

https://doi.org/10.1016/j.progpolymsci.2011.06.003